

Effect of particle oxidation, size and material on deposition during cold-spray: a peridynamics-based numerical investigation

Baihua Ren, Jun Song¹

Department of Mining and Materials Engineering, McGill University, Montréal, QC H3A 0C5, Canada

Abstract

Cold spray technology, distinguished by its unique ability to deposit particles in a solid state, offers unparalleled potential for applications such as coating, repair, and additive manufacturing. In this research, we employed a peridynamic modeling approach to systematically analyze the effects of key powder features on deposit properties. Notably, our model incorporates the explicit modeling of nanometer-sized oxide layers, providing a more accurate representation of real-world conditions. We assessed the influence of parameters such as particle size, oxidation conditions, and material type on crucial deposition indicators like critical velocity and compression ratio. Our results demonstrated excellent agreement with reported experimental data, affirming the effectiveness of the proposed numerical framework. Specifically, our findings highlighted that, for a given impact velocity, smaller particles, thicker oxide layers, and harder materials contribute to limited oxide removal and a decreased likelihood of successful adhesion. Additionally, we present a predictive framework that establishes a correlation between particle size and critical velocity, providing valuable insights for optimizing cold spray deposition parameters. This innovative approach not only enhances our understanding of the intricate interplay between powder features and deposit properties but also paves the way for a more efficient and cost-effective optimization process in cold spray applications.

Keywords: Peridynamics; Cold spray; Oxidation; Simulation; Powder

¹ Author to whom correspondence should be addressed. E-Mail : jun.song2@mcgill.ca

1. Introduction

In cold spraying (CS) ¹⁻⁵, micro-sized particles undergo acceleration within a preheated high-pressure gas stream, passing through a DeLaval-type nozzle ⁶⁻⁸ before reaching the substrate. These supersonic feedstock powders impact and adhere to the substrate through intensive plastic deformation. In recent years, CS has emerged as a new attractive coating technique in the domain previously heavily occupied by thermal spray. Unlike conventional thermal spraying methods characterized by severe oxidation, microstructure and phase changes due to thermal effects ^{9,10}, CS involves minimal heating of particles before impact, with impact velocities ranging from 200 to 1200 m/s. The colliding particles coalesce to form a dense coating with low oxide content. Bonding in CS arises from particle deformation during impact, a phenomenon intricately influenced by specific impact conditions and various powder characteristics, as extensively detailed in previous research ¹¹.

The optimization of coating microstructure and properties, tailored for each combination of substrate and coating materials, necessitates a series of spray experiments and corresponding characterizations. However, the absence of a comprehensive understanding of the mechanisms governing bonding and coating formation can render these optimization processes excessively time-consuming, costly, and, in some cases, unfeasible. The endeavor to fine-tune CS for specific materials has driven investigations into bonding mechanisms, drawing parallels between key characteristics of bonding in CS and processes such as explosive welding or shock wave powder compaction ¹². According to prevailing bonding theories ¹³, all metals and alloys exhibit the capability to form bonds when their clean surfaces come into contact within the range of interatomic forces. Nevertheless, the majority of metal surfaces undergo oxidation in ambient air, resulting in the development of a thin film that may gradually thicken over time ¹⁴. This native layer is recognized as a barrier to metallurgical bonding and necessitates breaking and displacement during cold spraying to establish fresh metal-on-metal interfacial contact. In cold spraying, it is widely acknowledged that plastic deformation occurring at high strain rates can lead to the partial removal of the native oxide layer. The substantial kinetic energy of the particles before impacting the substrate induces severe local plastic deformation in both the particle and the substrate, forming material jets at the particle-substrate interface ^{11,12}. However, metallic oxides, being inherently brittle, are incapable of undergoing such substantial plastic deformation. It is believed that the significant plastic deformation involved in jetting, disrupting the surface films into numerous debris, are responsible for creating gaps that expose fresh material ¹⁵⁻¹⁹. Therefore, achieving the appropriate particle impact velocity in CS is crucial, as it must be of sufficient magnitude to disrupt the thin native oxide layer present at the solid interfaces and facilitate contact between the two clean surfaces ^{15,16,18,20-25}. If the deformation level falls short, remnants of debris may persist at the interface, impeding local intimate contact ^{26,27}. The minimum particle velocity at which bonding occurs is termed the critical velocity and stands as an important parameter in cold spraying ^{11,12,28}. This velocity is dependent not only upon the properties of the sprayed material and substrate but also on powder size, morphology, composition, and the oxidation conditions of both the particle and substrate ^{29,30}.

Among all the variables mentioned, a major factor believed to significantly influence critical

velocity and final coating quality in CS is the native oxide layer³¹. Experiments have shown that for severely oxidized powders, the critical velocity is often determined by the oxides on the powder surface rather than by the material properties³². However, direct experimental observation of the oxide layer removal process during CS is challenging³³. Computational methods, on the other hand, offer a cost-effective means to assess the effect of the native oxide layer on deposit quality. To date, the finite element method (FEM), a potent and relatively efficient tool, has been the most extensively utilized method for studying particle deformation and coating characteristics in CS^{22,34-36}. However, the dynamic nature of the CS process often leads to instabilities and convergence issues in FEM simulations due to high strain rates and extreme plastic deformation^{9,31}. Moreover, traditional FEM models face challenges in treating damage, as their formulations are based on continuum mechanics, which is not suitable for discontinuities like cracks. Consequently, only a limited number of studies utilizing FEM approaches have incorporated the effects of oxide layers^{18,24,27}. To address the failure behavior of the oxide layer, specialized techniques like the element deletion method must be utilized, potentially leading to a violation of the conservation of mass and energy. Furthermore, in many FEM simulations, the thickness of considered oxide layers is on the order of several hundreds of nanometers^{9,18,24,27}, which is tens of orders of magnitude greater than the actual thickness of the native oxide film, due to computational limitations. Meshless methods like smoothed particle hydrodynamics (SPH) have also been utilized^{31,37,38}, demonstrating advantages in simulating particle impact problems by mitigating significant mesh distortion encountered in mesh-based methods. However, SPH also faces singularity problems due to the discontinuities resulting from oxide damage³⁹. Only a limited number of SPH studies directly modeled oxide layers, with a restricted thickness of hundreds of nanometers³¹. Meanwhile on the other side of the length scale spectrum, molecular dynamics (MD)⁴⁰⁻⁴² simulations have been employed to study high-velocity impact⁴³⁻⁴⁸. However, the complexity of implementing oxide layers in MD simulations limits their application. Only one of these studies represented the effects of a brittle layer on metallurgical bonding⁴³. While MD simulations provide valuable physical insights into the adhesion process, their feasibility is hampered as the simulated particles must be orders of magnitude smaller than the actual particles in CS. This limitation undermines the utility of MD as a predictive tool. These challenges have prompted researchers to adopt alternative numerical simulation approaches for studying CS parameters.

In a previous study by the authors, a peridynamics (PD)-based approach was employed to simulate copper (Cu) particles impacting a Cu substrate⁴⁹. The PD results successfully reproduced crucial factors such as splat deformation, coefficient of restitution, and the onset of jetting in both substrate and particle at varying impact velocities, consistent with experimental findings. These results demonstrated that the PD simulations can realistically portray actual CS conditions, and provide accurate description of the deformation and damage processes involved^{18,27,33}. On base of the PD approach established in our previous work⁴⁹, here we investigated the deformation behaviors of Cu and iron (Fe) particles upon impact on a matched substrate, in the presence of oxide.

The evolution and deformation behavior of oxide films on the surface of Cu and Fe particles are analyzed in detail to elucidate their effects on interfacial stress, temperature, and material

jetting as well as particle deposition. Furthermore, we comprehensively investigate the effects of particle size, material, and oxide layer thickness on CS impact and deposition processes. These parameters were chosen because they have a significant influence on the final performance of the deposit. Our work can serve as a valuable guide for optimizing deposition processes for various materials and guiding experimental testing of CS.

2. Methodology

In this section, the material model, PD simulations and oxide damage model are separately described in detail below. All the PD analyses in this research are conducted utilizing the open-source code Peridigm⁵⁰.

2.1. Material model

This paper concentrates on copper (Cu) and iron (Fe) particles impacting matching substrates. We utilize the Johnson-Cook (JC) plasticity model as the constitutive plasticity model, which incorporates the influences of strain, strain rate, and temperature. The Von-Mises equivalent stress derived from the JC model is expressed as follows⁵¹:

$$\sigma = [A + B\varepsilon^n][1 + C\ln\dot{\varepsilon}^*][1 - (T^*)^m] \quad (1)$$

$$T^* = \frac{T - T_{ref}}{T_m - T_{ref}} \quad (2)$$

Here, σ represents the flow stress, ε is the equivalent plastic strain (PEEQ), $\dot{\varepsilon}^*$ is the equivalent plastic strain rate normalized by the reference strain rate, T_{ref} is the threshold temperature allowing thermal softening of the particles, and T_m signifies the melting temperature of the metal. Constants A , B , C , n and m are experimentally derived, and T denotes the initial temperature of the particle, typically set to room temperature. Table 1 provides an overview of the material properties. These material properties are crucial for understanding the behavior of Cu and Fe particles during impact simulations.

Table 1 Material properties of copper (Cu)⁵¹, iron (Fe)⁵² and their corresponding oxides⁵³⁻⁵⁸.

Material (Metal) properties	Unit	Cu	Fe
Density	kg/m ³	8960	7890
Specific heat	J/kg – K	383	452
T_m	K	1356	1538
Young's modulus	GPa	124	207
Poisson's ratio	–	0.34	0.29
A	MPa	90	175
B	MPa	292	308
n	–	0.31	0.32
C	–	0.025	0.06
m	–	1.09	0.55
T_{ref}	K	298	298
Reference strain rate	1/s	1	1

Material (Oxide) properties	Unit	Cu Oxide	Fe Oxide
Density	kg/m ³	6000	5240
Young's modulus	GPa	126	220
Poisson's ratio	-	0.31	0.37
Fracture toughness	MPam ^{1/2}	5	2.05

2.2. Peridynamic model and simulation setup

Within the framework of PD, the material of interest is discretized into discrete points known as material points. These points interact through peridynamic bonds within a defined distance range denoted as δ . To simulate the deformation of the metal particle and substrate, a non-ordinary state-based peridynamic material model is employed. Concurrently, an ordinary state-based constitutive model is used to model the deformation and fracture of oxide layers. In PD, the introduction of material damage entails eliminating interactions among material points. Further details on the implementation of these specific peridynamic models, as well as the rationale behind their selection, can be found in our previous studies ⁵⁹.

Simulating single-particle impacts offers a valuable means of comprehending the influence of various feedstock parameters, providing computational efficiency compared to multi-particle models by avoiding complexities arising from interactions between incoming and deposited particles ^{9,60,61}. In our earlier work ⁴⁹, we demonstrated the efficacy of two-dimensional (2D) and three-dimensional (3D) peridynamic simulations in accurately depicting metal deformation, oxide evolution, separation, and removal. Leveraging the simplicity and robustness of the 2D model, and considering the axially symmetric nature of normal impact processes ^{12,62}, we prioritized computational efficiency. Specifically, our simulations utilized a 2D plane strain model where the degrees of freedom in the Z -direction were constrained for all material points ⁶². As shown in Fig. 1, the dimensions of the substrate (height H and width D) were maintained at approximately five times the particle diameter (d) to mitigate potential boundary effects ^{12,59,62}. It's important to note that 2D plane strain models have been utilized previously to investigate high strain rate deformation and predict critical velocities in CS ^{12,63,64}.

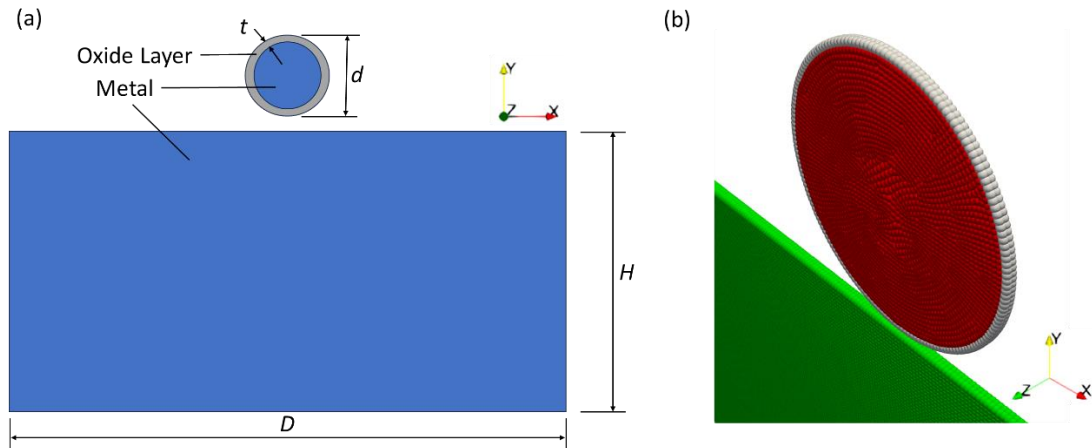


Fig. 1. (a) Schematic representation of the PD model used to simulate the CS process, where the particle and substrate materials are colored blue while the oxide layer on the impacting particle is colored gray. (b) The discretization used for particle, oxide layer and substrate.

2.3. Oxide damage model

This study utilizes the critical stretch criterion to simulate the damage behavior of oxide layers. It assumes that damage will occur when the bond stretch between two material points exceeds a critical value. Bond stretch is defined as follows ⁶⁵:

$$s = \frac{|\boldsymbol{\eta}| - |\boldsymbol{\xi}|}{|\boldsymbol{\xi}|} \quad (3)$$

The bond stretch is calculated as the difference between the current bond length $|\boldsymbol{\eta}|$ and the reference bond length $|\boldsymbol{\xi}|$, divided by the reference bond length $|\boldsymbol{\xi}|$. According to the critical stretch failure criterion, a peridynamic bond experiences irreversible breakage when its stretching surpasses a critical value denoted as s_0 . This critical stretch value is determined by the strain energy release rate G_0 , which can be experimentally quantified ^{66,67}

$$s_0 = \sqrt{\frac{G_0}{\left(\frac{6}{\pi}\mu + \left(\frac{16}{9\pi^2}\right)(\kappa - 2\mu)\right)\delta}} \quad (4)$$

Following bond failure, the inability to withstand loads results in the transfer of force to adjacent bonds, leading to a localized softening of the material response. This softening promotes the coalescence of broken bonds, leading to damage. With sustained loading, fracture may propagate through the material body ³⁹.

3. Results and discussion

3.1. Effect of oxide layer thickness

In the current study, we performed various simulations to evaluate the qualitative and quantitative effects of surface oxide film thickness on particle deformation and oxide removal. Here, and in Section 3.2 below, we focus primarily on Cu as a representative material system, while Sections 3.3 and 3.4 present results relevant to Cu and Fe material systems.

Figs. 2 and 3 depict the results for plastic strain and temperature evolution, respectively, simulated with oxide films of thickness $t = 2.5, 5, 10, 30,$ and 60 nm on the surfaces of $10 \mu\text{m}$ diameter Cu particles impacting on a Cu substrate. The analysis reveals that t has a little effect on the overall deformed particle shapes, particularly at low or moderate particle velocities. However, at high velocities where metal jetting may occur, e.g., at velocity of 650 m/s, it becomes evident that the degree of local metal jet is increasingly more restrained as the oxide thickness increases. In particular, we note that the metal jet is rendered non-existent at $t \geq 30$ nm, illustrated in Fig. 2 (l) and (o), and Fig. 3 (l) and (o). Earlier experimental investigations

involving Cu particles encapsulated in a substantial surface oxide layer (30 nm) impacting onto a Cu substrate hinted at a potential oxide constraint against local deformation on the particle side, as evidenced by the absence of hydrodynamic jetting near the critical velocity^{68,69}. In the present study, for the first time, we confirm such constraint of particle deformation using the PD framework.

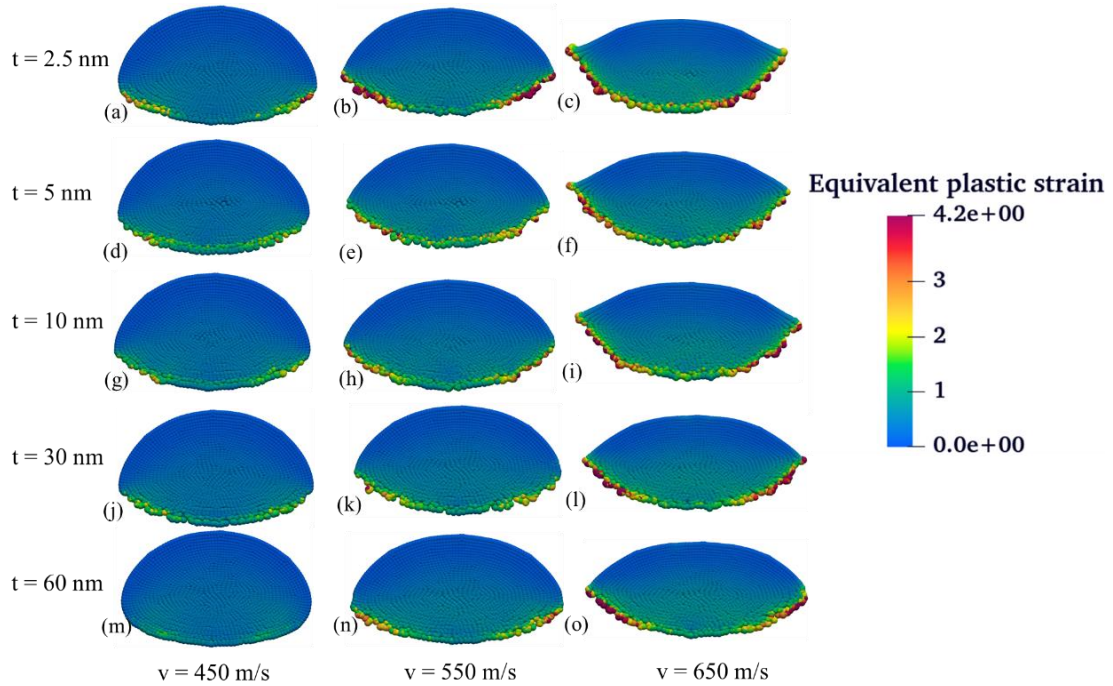


Fig. 2 Effect of surface oxide film thickness on the evolution of particle plastic strain, simulated at impact velocities of 450, 550, and 650 m/s, respectively. These simulations are conducted with Cu particles impacting Cu substrates, i.e., abbreviated as Cu-on-Cu impacts, where the metal particle is of diameter $d = 10 \mu\text{m}$. The color mapping indicates the magnitude of plastic strain.

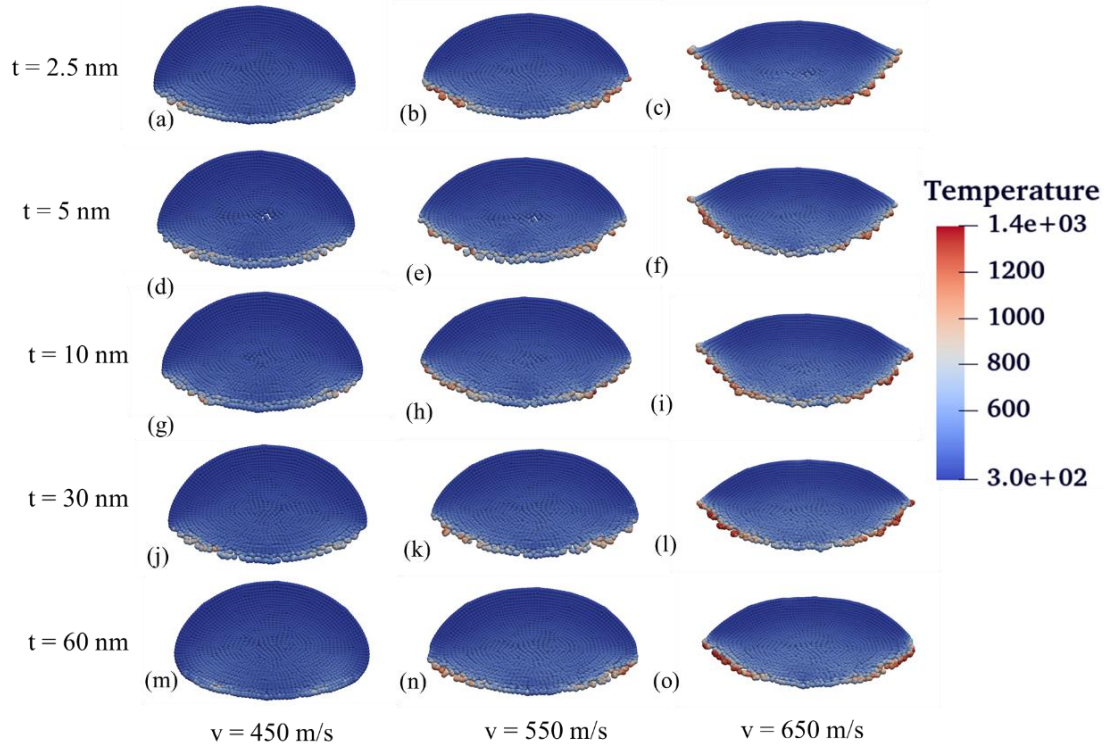


Fig. 3 Effect of surface oxide film thickness on the evolution of particle temperature, simulated at impact velocities of 450, 550, and 650 m/s, respectively. These simulations are conducted with Cu-on-Cu impacts, where the metal particle is of diameter $d = 10 \mu\text{m}$. The color mapping indicates the magnitude of temperature.

To provide a quantitative perspective on the effect of oxide thickness on particle deformation, Fig. 4 shows the maximum equivalent plastic strain (MEPS) and maximum temperature (MT) at different oxide thicknesses. It indicates that although MEPS and MT decrease with increasing oxide thickness at lower velocities, the importance of the oxide film on MEPS and MT diminishes at higher impact velocities. Specifically, at an impact velocity of 550 m/s, the MEPS and MT only exhibit a reduction from an oxide thickness of 30 nm to 60 nm. Meanwhile, at an impact velocity of 650 m/s, there is negligible change in both MEPS and MT. The disparate trends observed for MEPS and MT at various velocities may be attributed to the varying thickness of the oxide layer. Fig. 5 illustrates the final oxide distributions for particles with outer oxide layers of different thicknesses at three impact velocities: 450, 550, and 650 m/s. In all instances, sufficiently high velocities lead to the disruption and ejection of the oxide layer on the particle's bottom surface, facilitating intimate contact of freshly exposed metallic surfaces. However, these effects are considerably impeded at relatively low impact velocities (i.e., 450 m/s) as the thickness of the oxide layers increases. At this velocity, the entire oxide layer at the bottom part of the particle with a 60 nm oxide layer remains intact (Fig. 5 (m)), thereby limiting particle deformation. Additional insights are provided by the damage parameter contour within the oxide layer at the impact instances shown in Fig. 6. The constitutive model employed to characterize the brittle behavior of the oxide layer effectively describes its failure during impact. When considering a 60 nm oxide layer around a $10 \mu\text{m}$

diameter particle, a low velocity of 450 m/s fails to fully damage the oxide layer at the periphery where the most severe deformation is expected, in contrast to the oxide layers of the same particle with thinner thickness. At higher velocities, the oxide layer is disrupted on the particle's bottom surface for all considered oxide thicknesses, allowing for more substantial deformation. This suggests that the energy dissipated to break away the oxide films may be comparatively minimal, even with the thickest oxide layer of 60 nm, compared to the entire kinetic energy of the particle. Consequently, the MEPS and MT remain nearly unchanged at a velocity of 650 m/s, as shown in Fig. 4.

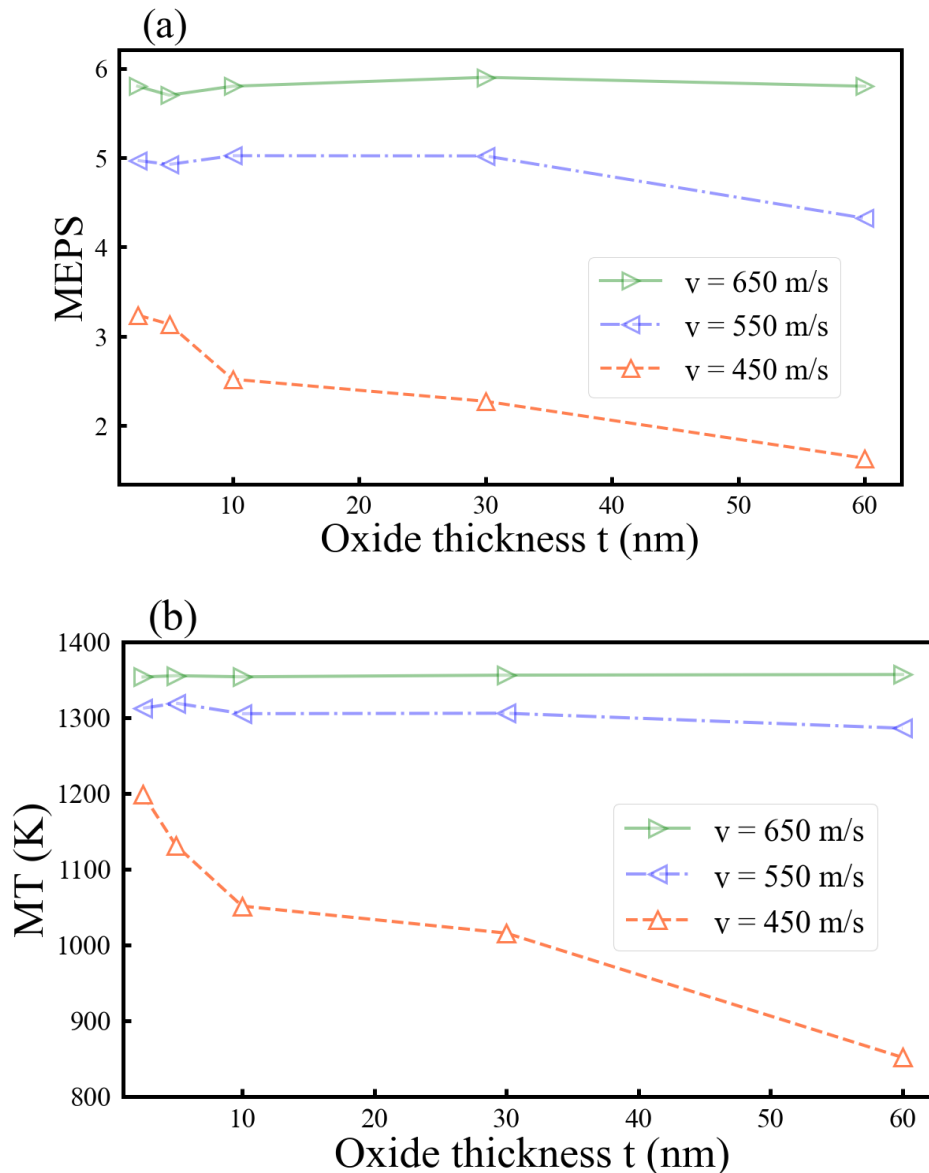


Fig. 4 Effect of surface oxide film thickness t on the particle (a) maximum equivalent plastic strain (MEPS), and (b) maximum temperature (MT) simulated with the impact velocity of 450, 550, and 650 m/s, respectively. The simulations are conducted with Cu-on-Cu impacts, where the metal particle is of diameter $d = 10 \mu\text{m}$.

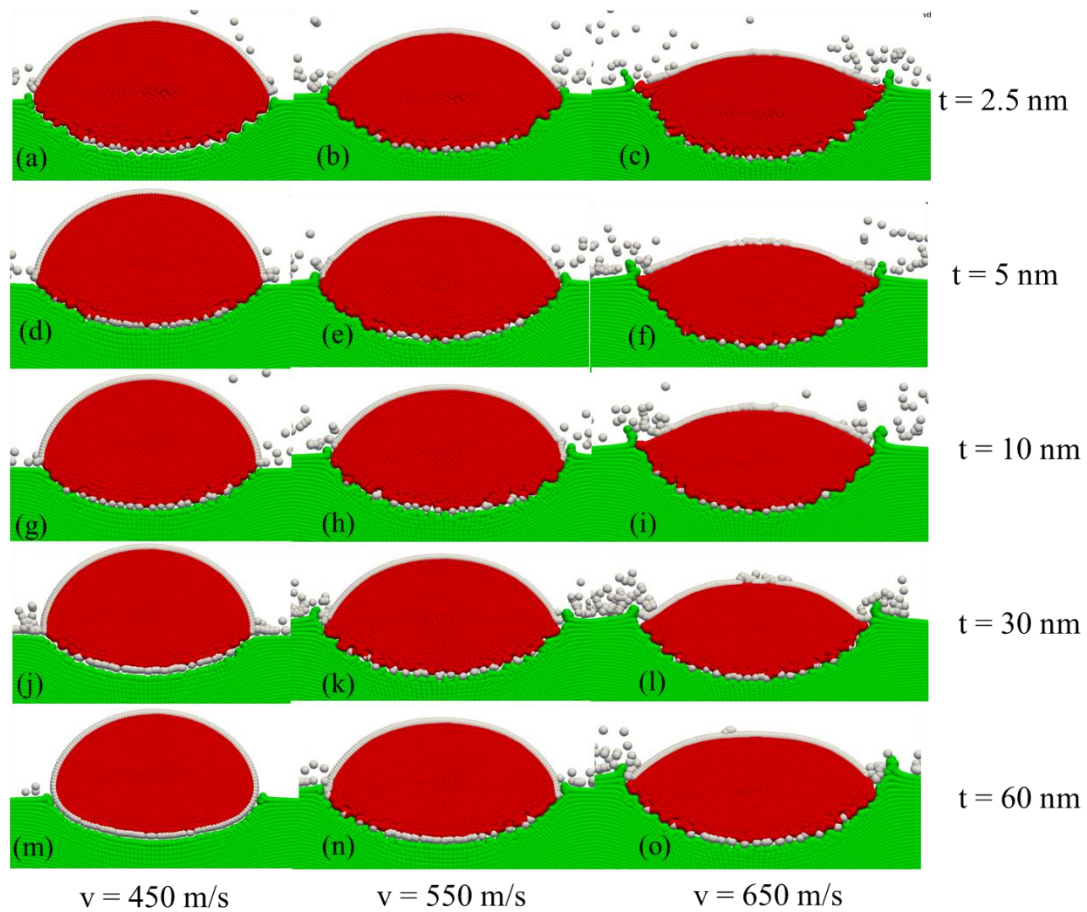


Fig. 5 Effect of surface oxide film thickness on the particle oxide distribution simulated with the impact velocity of 450, 550, and 650 m/s, respectively. These simulations are conducted with Cu-on-Cu impacts, where the metal particle is of diameter $d = 10 \mu\text{m}$. In the figure, green dots represent the substrate, white dots represent oxides, and red dots represent particles.

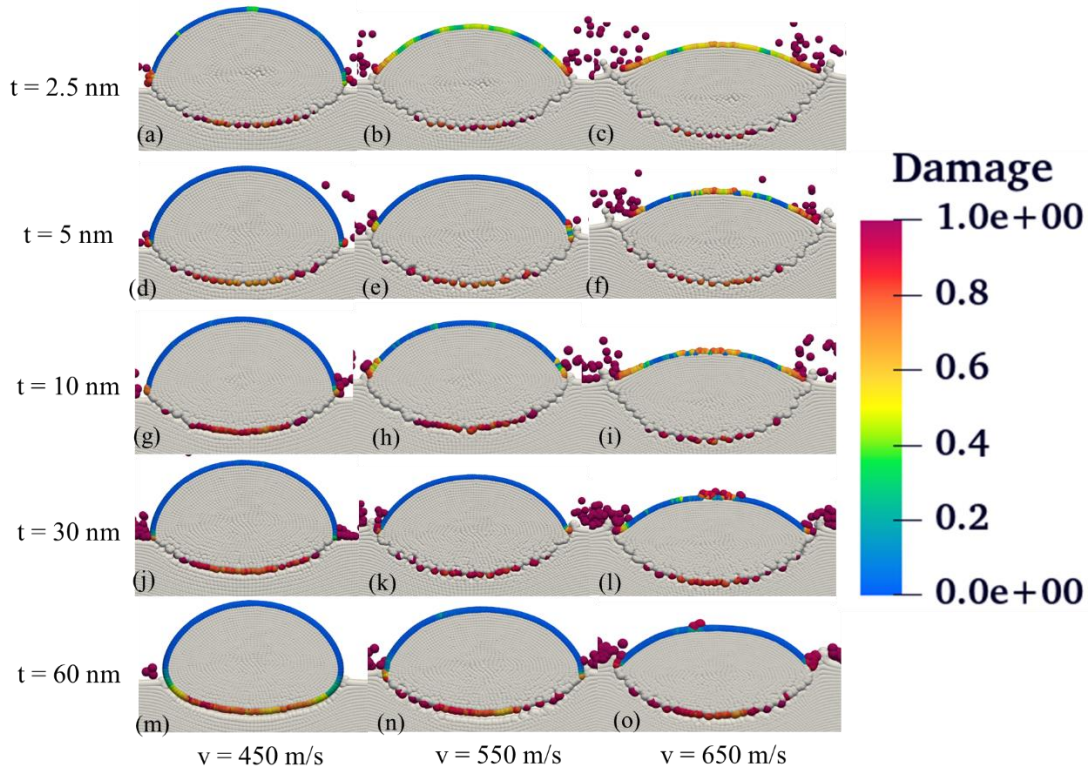


Fig. 6 Effect of surface oxide film thickness on the particle oxide damage simulated with the impact velocity of 450, 550, and 650 m/s, respectively. The simulations are conducted with Cu-on-Cu impacts, where the metal particle is of diameter $d = 10 \mu\text{m}$. The visualization uses blue and red colors to represent the extent of damage in oxides, while white color represents particles and substrates.

An intriguing observation in Fig. 5 and Fig. 6 is the initiation of jetting in cases with varying oxide layer thickness. Specifically, at an impact velocity of 450 m/s, the particle covered by a 2.5 nm oxide layer induces material jetting from the substrate at the contact edge (Fig. 5 (a)), whereas such jetting is not observed in cases with thicker oxide layers. On the other hand, particles at a velocity of 650 m/s exhibit jetting phenomena except for the one with a 60 nm oxide layer (Fig. 5 (o)). The initiations of material jetting are key indicators of contact behavior and bond strength during CS deposition, as observed in experimental results⁶⁹ and our previous numerical studies⁴⁹. Two cases are distinguished: one where jetting occurs only on the substrate, below the critical velocity, indicating limited metallurgical bonding due to insufficient oxide removal; and another where jetting occurs on both the substrate and particles, exceeding the critical velocity, indicating the removal of oxides in large quantities and resulting in the formation of high-strength metallic bonds. For the thinnest oxide layer of 2.5 nm, jetting on the substrate begins at 400-450 m/s, and jetting on both the substrate and particle starts between 550-600 m/s. In contrast, for the thickest oxide layer of 60 nm considered in this study, substrate jetting is not observed until 550-600 m/s, while particle jetting occurs at an impact velocity between 700-750 m/s. Simulation results for oxide thicknesses of 2.5 nm and 60 nm at the velocities where jetting is first observed are depicted in Fig. 7. For oxide thicknesses ranging from 5 nm to 30 nm, our findings indicate the onset of substrate-only jetting at velocities

between 500-550 m/s, and at 600-650 m/s, jetting is observed on both the substrate and the particle. As summarized in a previous study⁷⁰, for a 10 μm copper particle with a 2.5 nm oxide layer thickness, the critical velocity is determined to be 470 m/s. The initiation of substrate jetting at an impact velocity of 400-450 m/s, as obtained in the current study, appears reasonable. The critical velocity for a 10 μm particle with a thick oxide layer of 60 nm can be estimated to be in the range of 650-700 m/s, requiring further validation through experiments. Fig. 8 illustrates the effect of oxide layer thickness on the residual oxide at the interface after impact, showing that the thicker the oxide layer, the larger the volume of residual oxide, thereby increasing the critical velocity and adversely affecting the deposition. These findings are consistent with experimental studies⁷⁰. The substantial decrease in velocities necessary for initiating jetting from an oxide thickness of 5 nm to 2.5 nm corresponds well with previous experimental results, when considering copper oxide thickness ranging from 20 nm to 2 nm. This alignment indicates heightened sensitivity of the critical velocity to the thinning oxide layer⁷⁰. Furthermore, our simulations indicate a significant elevation in critical velocity from an oxide thickness of 30 nm to 60 nm, emphasizing the need for additional experimental validation.

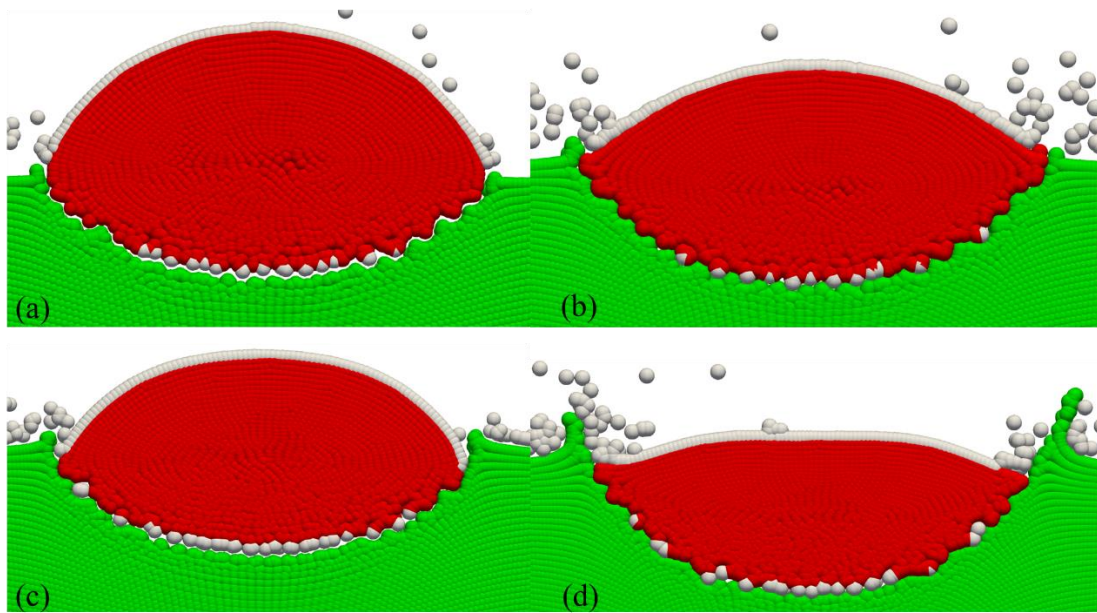


Fig. 7 Close-up views showing the effect of oxide layer thickness on the initiation of jetting from substrate and/or particle, illustrated by a few sample cases of different oxide thicknesses and particle velocities, being (a) $t = 2.5$ nm, $v = 450$ m/s (b) $t = 2.5$ nm, $v = 600$ m/s and (c) $t = 60$ nm, $v = 600$ m/s (d) $t = 60$ nm, $v = 750$ m/s. These simulations are conducted with Cu-on-Cu impacts, where the metal particle is of diameter $d = 10$ μm . In the figure, green dots represent the substrate, white dots represent oxides, and red dots represent particles.

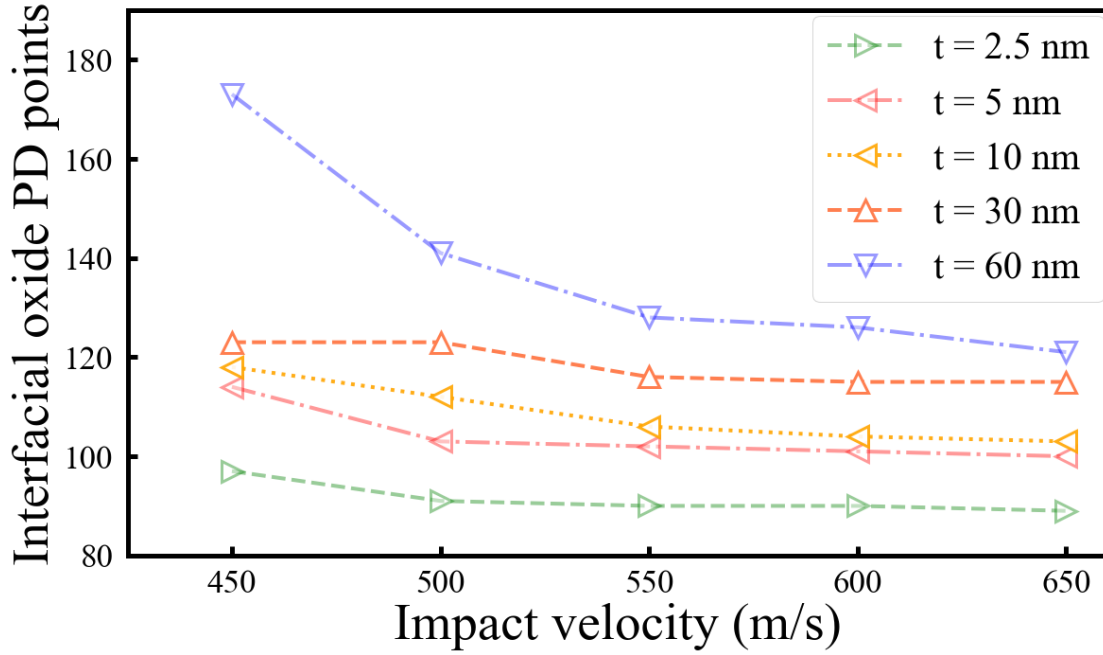


Fig. 8 The effect of oxide layer thickness t on the remaining oxide at the interface after impact. The simulations are conducted with Cu-on-Cu impacts, where the metal particle is of diameter $d = 10 \mu\text{m}$.

Previous investigations have highlighted that the residual oxide layer at the interface can hinder adhesion strength and reduce the extent of bonded surfaces^{26,71}. Our simulations demonstrate the fracture of the oxide layer into debris at the contact interfaces. Concurrently, the debris at the periphery is efficiently cleared by the metal jets. Consequently, the oxide films on particle surfaces undergo partial deposition into the coating, potentially influencing the microstructure and performance of the coating. Notably, an augmentation in oxide thickness correlates with an increased residual oxide layer at the interface, as illustrated in Fig. 8. This implies that a thicker oxide layer not only elevates the critical velocity but also compromises the quality of the coating.

3.2 Effect of particle size

The size effect plays a significant role in practical scenarios in CS applications where the particle size may vary widely, spanning more than an order of magnitude⁷². This variability in particle size is a crucial factor influencing various aspects of the process, such as particle velocity and temperature, and bonding in the coating⁷³. Schmidt et al.¹¹ and Dowding et al.⁷⁴ conducted studies that highlighted the particle size effect in cold spray, specifically in materials like Cu, 316 L stainless steel, pure Al, and Ti particles impacting matching substrates. Their experimental results indicated that an increase in the average particle diameter could lead to a lower critical velocity for the same materials in cold spraying. Computational methods have also been employed to explore the effect of particle size on critical velocities^{9,11,31,74,75}. These studies align with experimental findings, suggesting that finer particles tend to exhibit higher critical velocities. However, it's crucial to note that previous numerical simulation results might

lack reliability due to the potential influence of the oxide layer, which many studies did not consider. In cases where the oxide layer was indeed incorporated into models, its thickness was often several hundreds of nanometers, significantly thicker than the actual oxide thickness observed in experiments. Addressing this discrepancy is essential for more accurate simulations and a better understanding of the size effect in cold spray applications.

This section focuses on the impact of Cu particles on Cu substrates with an oxide layer of 10 nm. Examining Fig. 9, which illustrates the deformed shapes of particles ranging from 5 to 50 μm at various impact velocities, reveals a noteworthy observation. The deformed shapes of particles appear similar regardless of their sizes at the same impact velocity. This finding suggests a uniformity in deformation across different particle sizes, aligning with observations from previous FEM simulations⁷⁶. Further insights are provided in Fig. 10, showcasing the variation in compression ratios with particle impact velocity for various particle sizes. It becomes evident that the compression ratios exhibit similarities among different particle sizes when subjected to the same impact velocity. This consistency underscores the notion that, under the specified conditions, particle size variations do not significantly influence compression ratios at identical impact velocities.

As depicted in Fig. 9, the ratio of the oxide covered area to the oxide-free area at the particle-substrate interface exhibits a decreasing trend with an increase in particle size, observed at impact velocities of both 500 m/s and 600 m/s. This phenomenon occurs due to the expanded stretch experienced by the oxide surface as the particle diameter increases, consequently contributing to a reduction in critical velocity³¹. The larger particles, owing to their lower surface-to-volume ratios, maintain a lower oxide content volume percentage for a constant particle oxide layer thickness. In Fig. 11, the equivalent plastic strain (PEEQ) field distribution is presented for copper particles of sizes 5 μm , 10 μm , and 50 μm , after impact at 500 m/s on a copper substrate. The figure reveals that smaller particles with lower kinetic energy induce plastic deformation at a smaller magnitude, particularly evident in the strain at the particle-substrate interface, which remains below 5 for the 5 μm particle. This aligns with findings from previous FEM simulations¹¹. Conversely, the impact of a 50 μm particle results in significant plastic deformation, reaching levels of 5.5 or higher.

An essential indicator during the particle impact process is the initiation of discontinuities within the oxide, signifying complete damage. Our prior study revealed that this onset marks the exposure of fresh metal-to-metal contact, potentially influencing the rebound behavior of particles. As depicted in Fig. 12, this initiation occurs at 400 m/s for 10 μm copper particles, while 5 μm particles require an impact velocity of 500 m/s. This implies that larger particle diameters necessitate lower velocities for inducing bonding, affirming the correlation between particle diameter increase and a larger stretch on the oxide surface. Fig. 12 also illustrates the initiation of jetting on both the substrate and particle, along with the corresponding impact velocities for 5 μm and 10 μm copper particles. As discussed earlier, permanent bonding occurs within the velocity range between these two jetting onsets. For the 5 μm particle, the critical velocity exceeds 600 m/s, requiring an impact velocity of 700 m/s to achieve robust bonding, indicated by the onset of jetting on both the substrate and particle. Conversely, the 10 μm copper

particle exhibits a corresponding velocity range of 500-650 m/s, suggesting a lower critical velocity compared to the 5 μm particle.

Anticipated from previous studies ⁷⁴, the expectation that larger particles, endowed with higher kinetic energy, necessitate lower velocities to initiate jetting is confirmed. This paper uniquely underscores the explicit modeling of nanoscale oxide layers covering the particles, revealing a novel insight. It signifies, for the first time, that larger particles not only demand lower velocities for material jetting initiation but also for inducing damage and separation of the oxides, thus lower velocity for initiating the formation of metallurgical bonds.

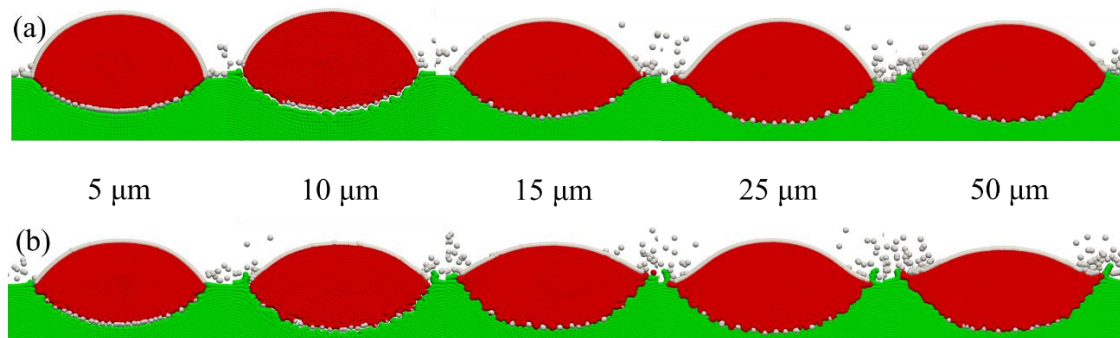


Fig. 9 The effect of particle size d on the remaining oxide at the interface after Cu-on-Cu impact, at the particle velocity of (a) 500 m/s and (b) 600 m/s. The metal particle diameters range from $d = 5 \mu\text{m}$ to $50 \mu\text{m}$. The metal oxide is of 10 nm thickness. In the figure, green dots represent the substrate, white dots represent oxides, and red dots represent particles.

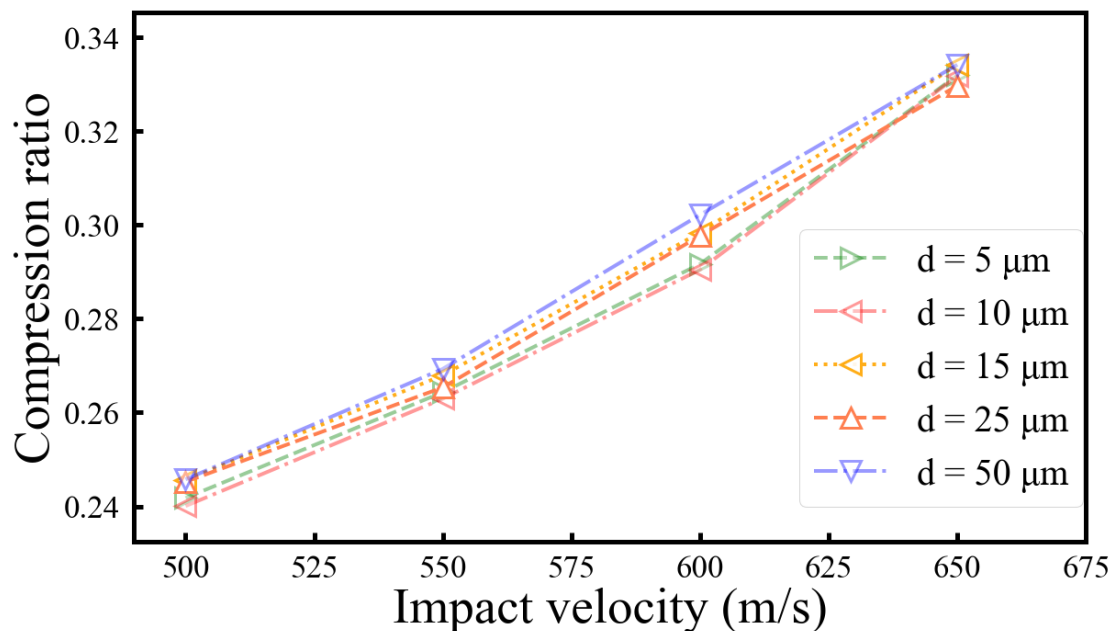


Fig. 10 The effect of particle size d on the compression ratio for Cu-on-Cu impact. The metal oxide is of $t = 10 \text{ nm}$ thickness.

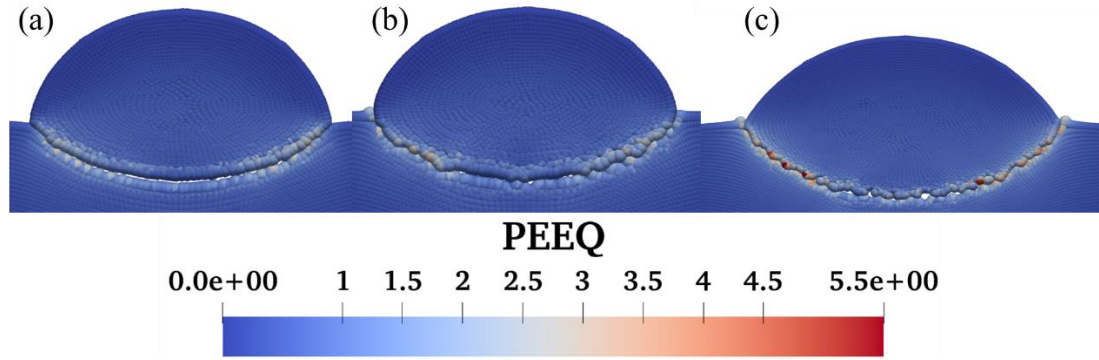


Fig. 11 Equivalent plastic strain (PEEQ) distribution for Cu-on-Cu impacts with particles of diameters of (a) 5 μm , (b) 10 μm and (c) 50 μm covered by a 10 nm thick oxide layer at velocity of 500 m/s. The color mapping indicates the magnitude of plastic strain.

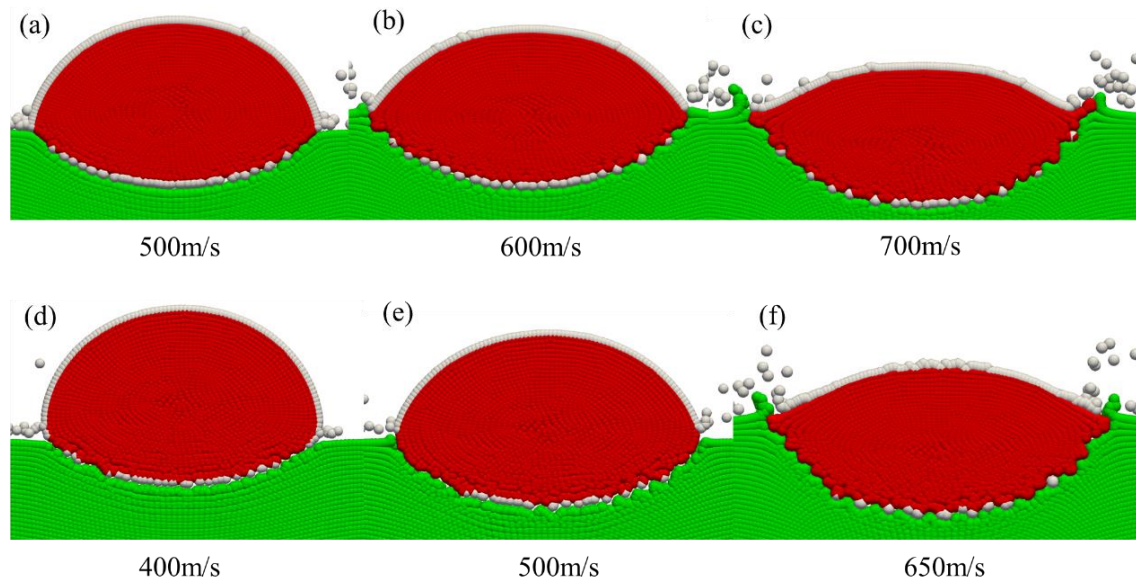


Fig. 12 The initiation of oxide discontinuity and jetting for Cu-on-Cu impact. Panels (a)-(c) depict particles with diameters of 5 μm , while panels (d)-(f) show particles with diameters of 10 μm , each covering a 10 nm oxide layer. In the figure, green dots represent the substrate, white dots represent oxides, and red dots represent particles.

3.3 Effect of particle material

The results in previous sections are based on a Cu particle impacting a Cu substrate. To gain more general understanding, we also consider the case of the material being Fe. Fig. 13 shows some sample side-to-side comparisons in terms of the final deformation and oxide distribution profiles obtained at varying velocities, for the two material systems. Examining the results, we note that though the general phenomenon of the oxide film breakage occurring at high velocities remains the same, there are some notable differences between the two material systems. For the Fe-on-Fe impact, the oxide film at the contact region is observed to be fully cracked when the impact velocity is beyond 550 m/s, while for the Cu-on-Cu impact, the oxide film cracks at a

lower velocity range of 450–500 m/s. Meanwhile, for the Fe-on-Fe impact, despite the high-velocity impact breaking up the oxide film, a more significant portion of cracked oxide persists at the interface due to the limited deformation, in comparison to the Cu-on-Cu case. Consequently, some oxide accumulates at the rim of the interface.

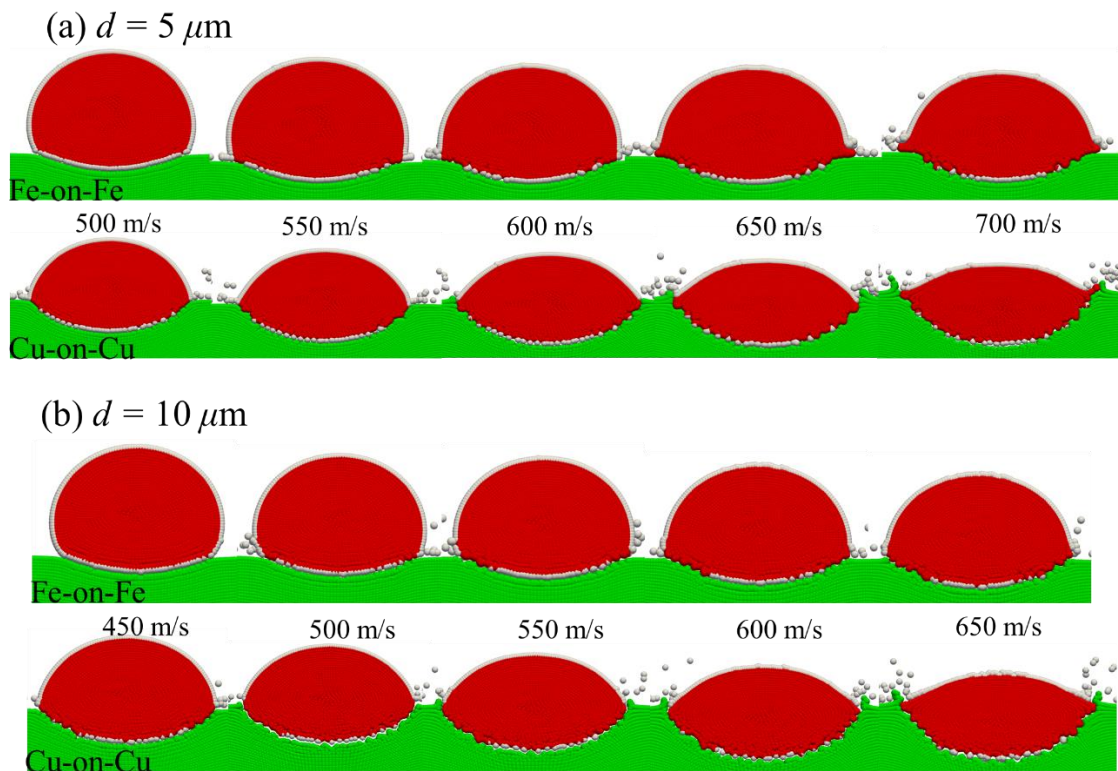


Fig. 13 The effect of material type with particle size: a) $d = 5 \mu\text{m}$ b) $d = 10 \mu\text{m}$, with 10 nm oxide. In the figure, green dots represent the substrate, white dots represent oxides, and red dots represent particles.

Increasing the impact velocity to 600 m/s reveals material jets at the substrate in the two Cu-Cu cases, i.e., the particle sizes $d = 5 \mu\text{m}$ and $10 \mu\text{m}$, aiding the expulsion of cracked oxides from the interface center. While some oxides remain at the interface, their quantity is smaller compared to the Fe-on-Fe cases. Also, it is clear to see from the final deformation profiles of the particle and substrate that at the same impact velocity the Cu-Cu interface exhibits a larger contact area than the Fe-Fe interface, attributed to more extensive deformation in the Cu-on-Cu impact. This can be further quantitatively supported by plotting the compression ratios for the two material systems, shown in Fig. 14(a) where higher compression ratios are observed for the Cu-on-Cu impact, and measuring the amount of oxide residue after impact, shown in Fig. 14(b) which demonstrates higher proportion of removed oxide for Cu-on-Cu impact. The above also suggests that, at the same impact velocity, it would be easier for soft particles against a soft substrate (e.g., Cu-on-Cu) to establish metallic bonding due to the larger interface area and, as shown in Fig. 14(b), more oxide removal, in contrast to hard particles against a hard substrate (e.g., Fe-on-Fe). It is also notable that for the Cu-Cu combination, the material jet

forms at the rim of the substrate crater, whereas for Fe-Fe, the substrate crater lacks a metal jet. In general, the material jet at the substrate crater rim contributes partially to removing cracked oxides, further enhancing the bonding strength of the Cu-Cu interface.

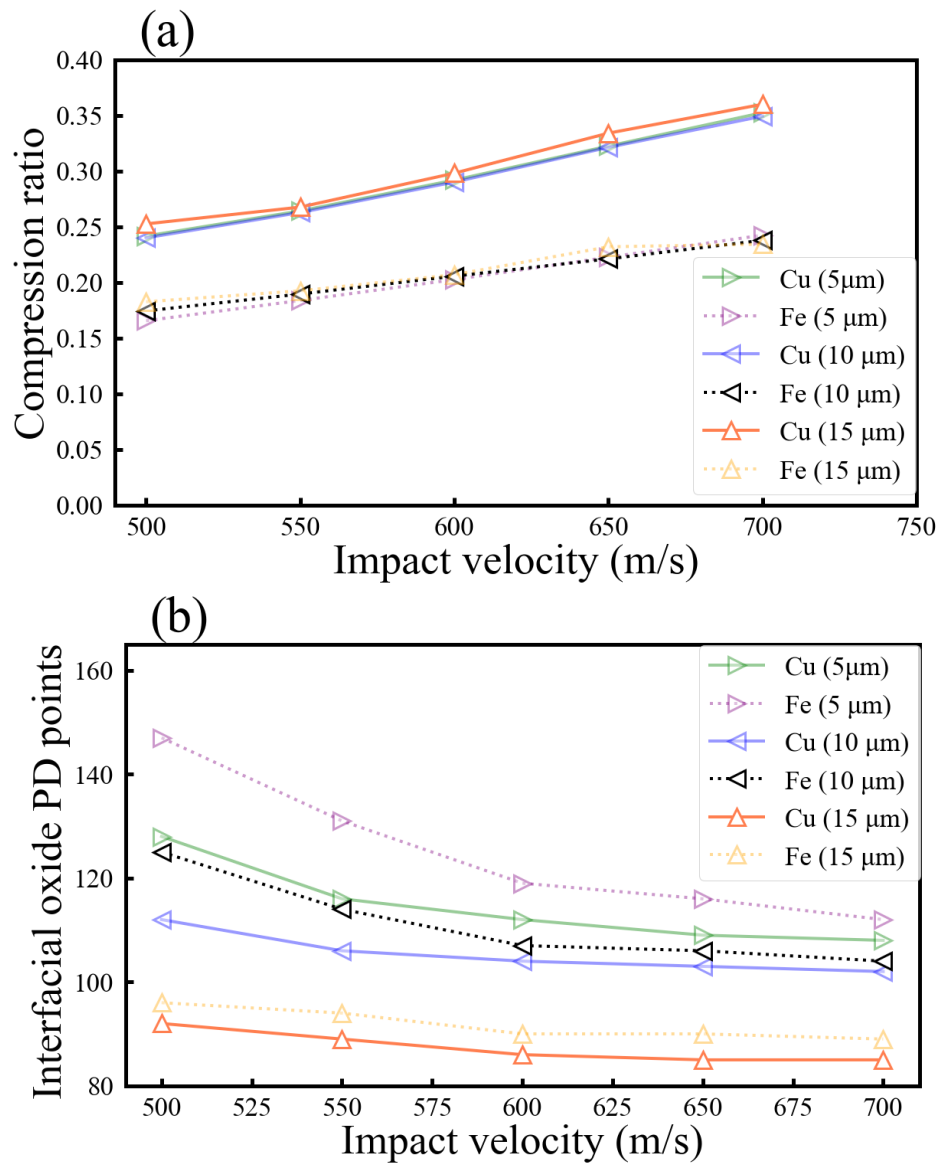


Fig. 14 (a) The compression ratio and (b) the amount of trapped oxide (namely amount of the interfacial oxide N_I) of Cu-on-Cu impacts and Fe-on-Fe impacts as the impact velocity varies from 500-700 m/s. The results shown here are for three representative particle sizes, being 5 μm, 10 μm and 15 μm, all with 10 nm oxide.

Additionally, we can see from Fig. 14(b) that as the velocity increases to 650 m/s and 700 m/s, despite more pronounced deformation of the particle and substrate, the amount of remaining oxide at the interface appears to show little change in either Cu-on-Cu or Fe-on-Fe cases, indicative of the quantity of remaining oxide being insensitive to the impact velocity at very high velocity range (i.e., from 650 m/s). Another observation from Fig. 14(b) is that the residual oxide for both Cu-on-Cu and Fe-on-Fe decreases with increasing particle size, and we argue that

this may represent some characteristics of the bonding phenomenon in CS, as to be further discussed in the next section.

3.4 Effect of particle size on the critical velocity

The results presented above give a clear indication that the particle size plays a role in affecting the material deformation and oxide breakage/removal processes, and naturally one would expect the particle size to affect the critical velocity. Experimental observations^{11,74} have indicated that the critical velocity, denoted as V_c , decreases as particle size increases, a relationship that can be mathematically described by a power law equation:

$$V_c \propto D^i \quad (5)$$

The previous studies^{11,74} determined that the size scaling index, denoted as i , is approximately -0.2 . In particular, for Cu, $i = -0.19$, for 316 L stainless steel, $i = -0.14$, for Al, $i = -0.19$, and for Ti, $i = -0.21$. In a related development, Hassani-Gangaraj et al.⁷⁷ formulated an approximation for the critical velocity relying on a hydrodynamic spall process:

$$\frac{V_c}{C_0} \approx \frac{2}{k} \times \frac{P_s}{B} \quad (6)$$

Here, C_0 represents the shock velocity, B is the bulk modulus, and P_s denotes the spall strength. Eq. (4) is founded on the dynamics of the shock wave emerging upon contact. When this shock wave reaches the particle's edge, it can initiate a release wave, leading to jetting if the stresses surpass the local spall strength of the material⁷⁷. Building on the groundwork laid by Hassani-Gangaraj et al.⁷⁷, Dowding et al.⁷⁴ proposed a mechanism explaining the particle size dependence using FEM. Their proposition suggested that adiabatic heating induced softening at the interface, thereby lowering the spall strength and reducing the barrier for jetting and bonding⁷⁴. Larger particles, endowed with higher kinetic energy, demand less impact velocity to initiate jetting. Their simulations yielded a satisfactory prediction for the impact bonding of Al and Ti, aligning well with experimental observations. Notably, the authors in²¹ did not incorporate considerations for oxide layers in their numerical models.

Indeed, impact-induced bonding for supersonic particles has been proposed to be closely linked to jetting phenomena^{12,21,70,77,78}. While the origin of jetting in the realm of cold spray remains a topic of debate, models grounded in adiabatic shear instability^{2,11,45} and hydrostatic pressure spall^{51,52} have been posited to explain the onset of jetting. It is widely accepted that jetting disrupts surface oxide films, regardless of the specific mechanism behind its formation. This disruption is considered a mechanism for cleaning the surface, facilitating pristine contact between the particle and substrate, and ultimately leading to bonding in cold spray^{12,79}. Consequently, this section focuses on the concept that, with an increase in particle diameter, the residual oxide volume decreases at the same impact velocity—an inference derived from Fig. 14(b). This implies that larger particles necessitate smaller impact velocities to achieve bonding.

To quantitatively investigate the effect of particle size, we initially conducted PD simulations akin to those depicted in Fig. 13. These simulations encompassed a variety of particle sizes for both Cu-on-Cu and Fe-on-Fe impacts, with a specific focus on quantifying the number of oxide material points situated at the particle/substrate interface, as illustrated in Fig. 14(b). To address potential discrepancies arising from discretization variances inherent in the PD models across the entire particle size range, we applied a practical normalization technique to the raw data,

$$N = \frac{N_I}{N_T} \quad (7)$$

where N_I represents the number of interfacial oxide PD points, and N_T is the total number of oxide material points covering the entire metal particle. This normalization is considered meaningful as it offsets the fluctuation of N_I across various particle sizes, since N_I is expected to increase as the particle size grows, reflecting the enlargement of the contact region. The parameter N thus represents the portion of the total oxide encapsulated within the interface. From Fig. 15, we can see that for a particular particle size, N varies with impact velocity, increasing monotonically as the velocity grows prior to the onset of oxide discontinuity, which aligns with our expectations. On the other hand, N decreases with increasing velocity after the onset of discontinuity, indicating the onset of the oxide cleaning effect. Further in Figs. 16(a) - (d), it is apparent that the parameter N maintains nearly a constant value for all tested Fe and Cu particle sizes before the onset of oxide discontinuity (at low impact velocities, e.g., 150 m/s and 300 m/s). Meanwhile, N_I exhibits a monotonically increasing trend as the particle size grows, in alignment with our expectation. This confirmation establishes N as a reliable indicator of the extent of damage and oxide removal, since changes in N are solely attributable to the crushing and cleaning effects caused by particle deformation and are independent of particle size.

On the other hand, once the impact velocity is sufficient to induce oxide discontinuity, e.g., at high impact velocities of 450 m/s and 550 m/s as shown in Fig. 17, N is observed to monotonically decrease as the particle size increases. In particular, the evolution of N as a function of the particular size exhibits a power-law form. Fitting the data to the power-law form, expressed as $N = N_0 D^\alpha$ with N_0 and α being fitting parameters, we obtained the values of N_0 and α for Fe-on-Fe and Cu-on-Cu systems. The fitted equations for Fe-on-Fe impacts are: $0.3663 \times D^{-0.199}$ for an impact velocity of 550 m/s and $0.3327 \times D^{-0.192}$ for an impact velocity of 600 m/s. For Cu-on-Cu impacts, the equations are: $0.3942 \times D^{-0.236}$ for an impact velocity of 450 m/s and $0.3662 \times D^{-0.225}$ for an impact velocity of 500 m/s.

We see that α exhibits a more negative value for Cu-on-Cu than that for Fe-on-Fe. This is consistent with our previous observations. As discussed previously, if we take the oxide removal as the critical condition for establishing of metallic contact and thus achievement of bonding, then the parameter α would have direct correspondence to the parameter i in Eq. (5). Indeed we can see that the obtained values of α are consistent with the observations made by Schmidt et al.¹¹, which found $i = -0.14$ and $i = -0.19$ for stainless steel and Cu respectively. Thus, we assert that the proposed mechanism for the size effect encapsulates the

fundamental physics: larger particles result in less oxide-covered interfaces, thereby requiring less impact velocities to achieve bonding conditions. It's noteworthy that the selection of impact velocities depicted in Fig. 17 is contingent upon the minimum velocity at which the cleaning effect begins to manifest for the smallest particle size investigated in this study (5 μm). Accordingly, we have chosen the impact velocity to be 450 and 500 m/s for Cu-on-Cu impacts and 550 and 600 m/s for Fe-on-Fe impacts.

The data presented in Fig. 17 represents the first numerical attempt, to our knowledge, to elucidate the particle size effect in impact bonding, considering the influence of the oxide layer, a crucial factor in the CS process. It is worth noting that previous mechanisms on bonding, e.g., the mechanism proposed by Dowding et al. ⁷⁴, are often hinged on the assumption of bonding being closely linked to jetting, which is considered a spall process. While in our current study, through explicit modeling of oxide layer deformation and damage, we offer a direct explanation for the particle size effect, irrespective of the specific jetting mechanism. Notably, this methodology remains relevant in scenarios or materials where particle jetting isn't visibly present even at critical velocities. For example, in instances where Cu particles don't exhibit jetting signs at or slightly above the corresponding critical velocity ^{68,69}, the size effect would still exist, and may be attributed to oxide breakage and removal resulting from plastic deformation, notwithstanding the absence of an apparent spall process leading to material jetting.

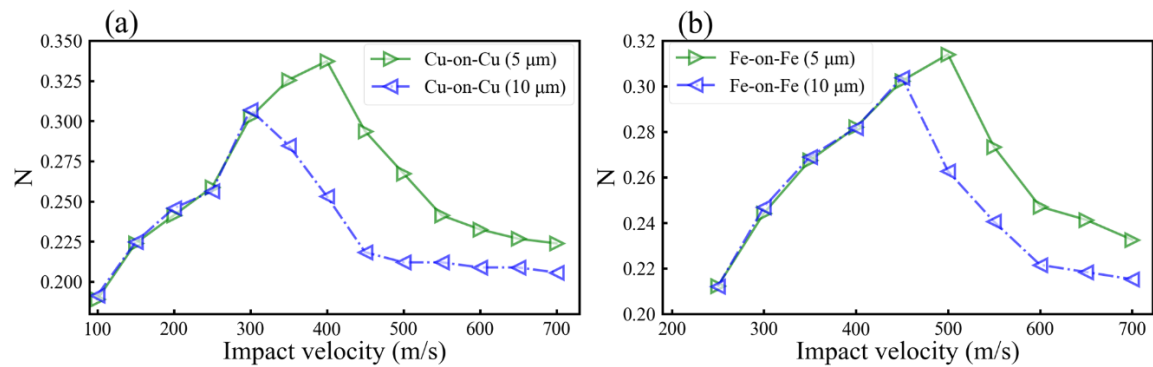


Fig. 15 Normalized number of trapped oxides N of a) Cu-on-Cu and b) Fe-on-Fe impacts as a function of the particle velocity. The oxide is of 10 nm thickness.

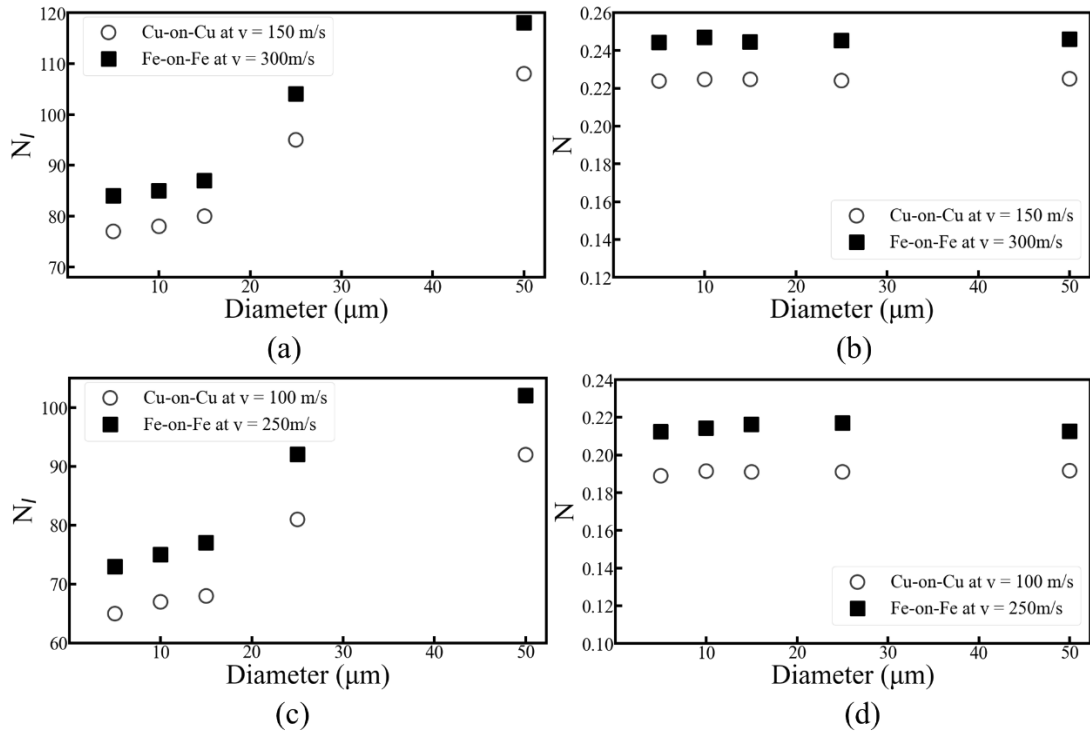


Fig. 16 Peridynamic results for: a) and c) number of trapped oxides for Cu-on-Cu impacts at 150 m/s, and Fe-on-Fe impacts at 300 m/s, b) and d) normalized number of trapped oxides for Cu-on-Cu impacts at 100 m/s, and Fe-on-Fe impacts at 250 m/s as a function of the particle size.

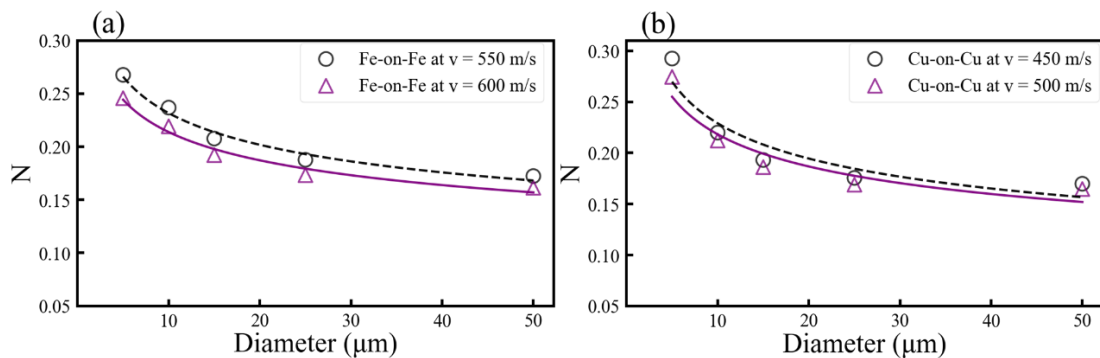


Fig. 17 Normalized number of trapped oxides N of a) Fe on Fe and b) Cu on Cu as a function of the particle size. The oxide is of 10 nm thickness.

4. Conclusion

Explicitly considering an oxide layer around the metal particle, this study systematically studied the material deformation and oxide fracture process of a single metal particle cold-sprayed to impact a matched metal substrate, using peridynamics (PD) simulations. Our results have led to several findings, summarized below:

(a) The oxide film on the particle surface was shown to affect the plastic strain and temperature at the interface, especially at lower velocities. Increasing oxide thickness results in restriction of particle deformation at the interface, making it difficult to induce material jetting. A thick

oxide layer also hinders the cracking and partial removal of the oxide, requiring higher impact velocities to establish metal-to-metal contact. Consequently, the critical velocity increases as the oxide thickness grows, consistent with experimental results.

(b) A thicker oxide layer also leads to larger volume of broken oxides at the interface, which may become embedded into the resulting coating, thus deteriorating the bonding strength of the deposited particles.

(c) At the same impact velocity, the compression ratios of different particle sizes are similar, indicating uniform deformation.

(d) Larger particles require lower velocities to cause oxide damage and material jetting. They also produce smaller oxide coverage at the interface compared to finer particles under the same conditions, indicating a lower critical velocity. This study shows that, based on quantified interfacial oxides, the size scaling exponent of impact bonding is approximately -0.19 for iron and -0.23 for copper, consistent with previous findings.

(e) Under the same conditions, soft-on-soft impacts may be more beneficial for metal bonding compared to hard-on-hard impacts. This is due to the larger interfacial area and higher proportion of oxide-free contact area, which result from increased deformation. This helps reduce the critical velocity of soft particles impacting a soft substrate.

This study underscores the importance of considering the influence of oxides on the deformation behavior of sprayed metal particles for reliable simulations. Additionally, it demonstrates that numerical methods can help optimize deposition processes for various materials and guide experimental testing, thereby saving time and costs.

Acknowledgement

The authors acknowledge the financial support from the Natural Sciences and Engineering Research Council of Canada (Grant #: NSERC RGPIN-2023-03628 and NETPG 493953-16) and McGill Engineering Doctoral Award (MEDA). The authors would also like to acknowledge the Digital Research Alliance of Canada for providing computing resources.

References

- 1 Irissou, E., Legoux, J.G., Ryabinin, A.N. et al. Review on Cold Spray Process and Technology: Part I—Intellectual Property. *J Therm Spray Tech* **17** (2008).
- 2 Lee, C. & Kim, J. Microstructure of Kinetic Spray Coatings: A Review. *Journal of Thermal Spray Technology* **24**, 592-610, doi:10.1007/s11666-015-0223-5 (2015).
- 3 Pathak, S. & Saha, G. C. Development of Sustainable Cold Spray Coatings and 3D Additive Manufacturing Components for Repair/Manufacturing Applications: A Critical Review. *Coatings* **7**, 122 (2017).
- 4 Moridi, A., Hassani-Gangaraj, S. M., Guagliano, M. & Dao, M. Cold spray coating: review of material systems and future perspectives. *Surface Engineering* **30**, 369-395, doi:10.1179/1743294414Y.0000000270 (2014).
- 5 Yin, S. et al. Cold spray additive manufacturing and repair: Fundamentals and applications. *Additive Manufacturing* **21**, 628-650, doi:<https://doi.org/10.1016/j.addma.2018.04.017> (2018).
- 6 Papyrin, A., Kosarev, V., Klinkov, S., Alkimov, A. & Fomin, V. in *Cold Spray Technology* (eds Anatolii Papyrin et al.) 33-118 (Elsevier, 2007).
- 7 Champagne, V. K. in *The Cold Spray Materials Deposition Process* (ed Victor K. Champagne) 1-7 (Woodhead Publishing, 2007).
- 8 Villafuerte, J. *Modern cold spray: materials, process, and applications*. (Springer, 2015).
- 9 Ardeshiri Lordejani, A., Colzani, D., Guagliano, M. & Bagherifard, S. An inclusive numerical framework to assess the role of feedstock features on the quality of cold spray deposits. *Materials & Design* **224**, 111374, doi:<https://doi.org/10.1016/j.matdes.2022.111374> (2022).
- 10 Karthikeyan, J. in *The Cold Spray Materials Deposition Process* (ed Victor K. Champagne) 62-71 (Woodhead Publishing, 2007).
- 11 Schmidt, T., Gärtner, F., Assadi, H. & Kreye, H. Development of a generalized parameter window for cold spray deposition. *Acta Materialia* **54**, 729-742, doi:<https://doi.org/10.1016/j.actamat.2005.10.005> (2006).
- 12 Assadi, H., Gärtner, F., Stoltenhoff, T. & Kreye, H. Bonding mechanism in cold gas spraying. *Acta Materialia* **51**, 4379-4394, doi:[https://doi.org/10.1016/S1359-6454\(03\)00274-X](https://doi.org/10.1016/S1359-6454(03)00274-X) (2003).
- 13 Bay, N. Cold Pressure Welding—The Mechanisms Governing Bonding. *Journal of Engineering for Industry* **101**, 121-127, doi:10.1115/1.3439484 (1979).
- 14 Lienhard, J. et al. Surface oxide and hydroxide effects on aluminum microparticle impact bonding. *Acta Materialia* **197**, 28-39, doi:<https://doi.org/10.1016/j.actamat.2020.07.011> (2020).
- 15 Assadi, H., Kreye, H., Gärtner, F. & Klassen, T. Cold spraying – A materials perspective. *Acta Materialia* **116**, 382-407, doi:<https://doi.org/10.1016/j.actamat.2016.06.034> (2016).
- 16 Ichikawa, Y., Tokoro, R., Tanno, M. & Ogawa, K. Elucidation of cold-spray deposition mechanism by auger electron spectroscopic evaluation of bonding interface oxide film. *Acta Materialia* **164**, 39-49, doi:<https://doi.org/10.1016/j.actamat.2018.09.041> (2019).
- 17 Xie, Y. et al. New insights into the coating/substrate interfacial bonding mechanism in cold spray. *Scripta Materialia* **125**, 1-4, doi:<https://doi.org/10.1016/j.scriptamat.2016.07.024>

- (2016).
- 18 Yin, S., Wang, X., Li, W., Liao, H. & Jie, H. Deformation behavior of the oxide film on the surface of cold sprayed powder particle. *Applied Surface Science* **259**, 294-300, doi:<https://doi.org/10.1016/j.apsusc.2012.07.036> (2012).
- 19 Grujicic, M., Saylor, J. R., Beasley, D. E., DeRosset, W. S. & Helfritsch, D. Computational analysis of the interfacial bonding between feed-powder particles and the substrate in the cold-gas dynamic-spray process. *Applied Surface Science* **219**, 211-227, doi:[https://doi.org/10.1016/S0169-4332\(03\)00643-3](https://doi.org/10.1016/S0169-4332(03)00643-3) (2003).
- 20 Chen, C. *et al.* On the role of oxide film's cleaning effect into the metallurgical bonding during cold spray. *Materials Letters* **210**, 199-202, doi:<https://doi.org/10.1016/j.matlet.2017.09.024> (2018).
- 21 Grujicic, M., Zhao, C. L., DeRosset, W. S. & Helfritsch, D. Adiabatic shear instability based mechanism for particles/substrate bonding in the cold-gas dynamic-spray process. *Materials & Design* **25**, 681-688, doi:<https://doi.org/10.1016/j.matdes.2004.03.008> (2004).
- 22 Li, W.-Y. & Gao, W. Some aspects on 3D numerical modeling of high velocity impact of particles in cold spraying by explicit finite element analysis. *Applied Surface Science* **255**, 7878-7892, doi:<https://doi.org/10.1016/j.apsusc.2009.04.135> (2009).
- 23 Li, W. Y. *et al.* Significant influences of metal reactivity and oxide films at particle surfaces on coating microstructure in cold spraying. *Applied Surface Science* **253**, 3557-3562, doi:<https://doi.org/10.1016/j.apsusc.2006.07.063> (2007).
- 24 Kim, K., Li, W. & Guo, X. Detection of oxygen at the interface and its effect on strain, stress, and temperature at the interface between cold sprayed aluminum and steel substrate. *Applied Surface Science* **357**, 1720-1726, doi:<https://doi.org/10.1016/j.apsusc.2015.10.022> (2015).
- 25 Stoltenhoff, T., Borchers, C., Gärtner, F. & Kreye, H. Microstructures and key properties of cold-sprayed and thermally sprayed copper coatings. *Surface and Coatings Technology* **200**, 4947-4960, doi:<https://doi.org/10.1016/j.surfcoat.2005.05.011> (2006).
- 26 Kang, K., Yoon, S., Ji, Y. & Lee, C. Oxidation dependency of critical velocity for aluminum feedstock deposition in kinetic spraying process. *Materials Science and Engineering: A* **486**, 300-307, doi:<https://doi.org/10.1016/j.msea.2007.09.010> (2008).
- 27 Li, W.-Y., Liao, H., Li, C.-J., Bang, H.-S. & Coddet, C. Numerical simulation of deformation behavior of Al particles impacting on Al substrate and effect of surface oxide films on interfacial bonding in cold spraying. *Applied Surface Science* **253**, 5084-5091, doi:<https://doi.org/10.1016/j.apsusc.2006.11.020> (2007).
- 28 Assadi, H. *et al.* On Parameter Selection in Cold Spraying. *Journal of Thermal Spray Technology* **20**, 1161-1176, doi:10.1007/s11666-011-9662-9 (2011).
- 29 Koivuluoto, H. & Vuoristo, P. Effect of Powder Type and Composition on Structure and Mechanical Properties of Cu + Al₂O₃ Coatings Prepared by using Low-Pressure Cold Spray Process. *Journal of Thermal Spray Technology* **19**, 1081-1092, doi:10.1007/s11666-010-9491-2 (2010).
- 30 Wong, W. *et al.* Effect of Particle Morphology and Size Distribution on Cold-Sprayed Pure Titanium Coatings. *Journal of Thermal Spray Technology* **22**, 1140-1153, doi:10.1007/s11666-013-9951-6 (2013).
- 31 Hemeda, A. A. *et al.* Particle-based simulation of cold spray: Influence of oxide layer on

- impact process. *Additive Manufacturing* **37**, 101517, doi:10.1016/j.addma.2020.101517 (2021).
- 32 Li, C. J. *et al.* Influence of Spray Materials and Their Surface Oxidation on the Critical Velocity in Cold Spraying. *Journal of Thermal Spray Technology* **19**, 95-101, doi:10.1007/s11666-009-9427-x (2010).
- 33 Rahmati, S., Veiga, R. G. A., Zúñiga, A. & Jodoin, B. A Numerical Approach to Study the Oxide Layer Effect on Adhesion in Cold Spray. *Journal of Thermal Spray Technology* **30**, 1777-1791, doi:10.1007/s11666-021-01245-4 (2021).
- 34 Ghelichi, R., Bagherifard, S., Guagliano, M. & Verani, M. Numerical simulation of cold spray coating. *Surface and Coatings Technology* **205**, 5294-5301, doi:<https://doi.org/10.1016/j.surfcoat.2011.05.038> (2011).
- 35 Song, X. *et al.* Residual stresses in single particle splat of metal cold spray process – Numerical simulation and direct measurement. *Materials Letters* **230**, 152-156, doi:<https://doi.org/10.1016/j.matlet.2018.07.117> (2018).
- 36 Xie, J., Nélias, D., Walter-Le Berre, H., Ogawa, K. & Ichikawa, Y. Simulation of the Cold Spray Particle Deposition Process. *Journal of Tribology* **137**, 041101, doi:10.1115/1.4030257 (2015).
- 37 Li, W.-Y., Yin, S. & Wang, X.-F. Numerical investigations of the effect of oblique impact on particle deformation in cold spraying by the SPH method. *Applied Surface Science* **256**, 3725-3734, doi:<https://doi.org/10.1016/j.apsusc.2010.01.014> (2010).
- 38 Gnanasekaran, B. *et al.* A Smoothed Particle Hydrodynamics (SPH) procedure for simulating cold spray process - A study using particles. *Surface and Coatings Technology* **377**, 124812, doi:<https://doi.org/10.1016/j.surfcoat.2019.07.036> (2019).
- 39 Yang, S., Gu, X., Zhang, Q. & Xia, X. Bond-associated non-ordinary state-based peridynamic model for multiple spalling simulation of concrete. *Acta Mechanica Sinica* **37**, 1104-1135, doi:10.1007/s10409-021-01055-5 (2021).
- 40 Hollingsworth, S. A. & Dror, R. O. Molecular Dynamics Simulation for All. *Neuron* **99**, 1129-1143, doi:10.1016/j.neuron.2018.08.011 (2018).
- 41 Schneider, R., Sharma, A. R. & Rai, A. in *Computational Many-Particle Physics* (eds H. Fehske, R. Schneider, & A. Weiße) 3-40 (Springer Berlin Heidelberg, 2008).
- 42 Hospital, A., Goñi, J. R., Orozco, M. & Gelpí, J. L. Molecular dynamics simulations: advances and applications. *Adv Appl Bioinform Chem* **8**, 37-47, doi:10.2147/aabc.S70333 (2015).
- 43 Pereira, L. M., Rahmati, S., Zúñiga, A., Jodoin, B. & Veiga, R. G. A. Atomistic study of metallurgical bonding upon the high velocity impact of fcc core-shell particles. *Computational Materials Science* **186**, 110045, doi:<https://doi.org/10.1016/j.commatsci.2020.110045> (2021).
- 44 Gao, H., Zhao, L., Zeng, D. & Gao, L. in *2007 First International Conference on Integration and Commercialization of Micro and Nanosystems*. 195-202.
- 45 Gao, H., Liu, C. & Song, F. H. Molecular Dynamics Simulation of the Influence Factors of Particle Depositing on Surface during Cold Spray. *Advanced Materials Research* **652-654**, 1916-1924, doi:10.4028/www.scientific.net/AMR.652-654.1916 (2013).
- 46 Joshi, A. & James, S. Molecular dynamics simulation study of cold spray process. *Journal of Manufacturing Processes* **33**, 136-143, doi:<https://doi.org/10.1016/j.jmapro.2018.05.005> (2018).

- 47 Joshi, A. & James, S. Molecular Dynamics Simulation Study on Effect of Process Parameters on Coatings during Cold Spray Process. *Procedia Manufacturing* **26**, 190-197, doi:<https://doi.org/10.1016/j.promfg.2018.07.026> (2018).
- 48 Malama, T., Hamweendo, A. & Botef, I. Molecular Dynamics Simulation of Ti and Ni Particles on Ti Substrate in the Cold Gas Dynamic Spray (CGDS) Process. *Materials Science Forum* **828-829**, 453-460, doi:10.4028/www.scientific.net/MSF.828-829.453 (2015).
- 49 Ren, B. & Song, J. Peridynamics simulation of microparticle impact: Deformation, jetting, and the influence of surface oxide layer *Under Review* (2024).
- 50 Parks, M. L., Littlewood, D. J., Mitchell, J. A. & Silling, S. A. Peridigm users' guide. V1.0.0. Report No. SAND2012-7800 United States 10.2172/1055619 SNL English, Medium: ED; Size: 38 p. (; Sandia National Laboratories, 2012).
- 51 Johnson, G. R. & Cook, W. H. Fracture characteristics of three metals subjected to various strains, strain rates, temperatures and pressures. *Engineering Fracture Mechanics* **21**, 31-48, doi:[https://doi.org/10.1016/0013-7944\(85\)90052-9](https://doi.org/10.1016/0013-7944(85)90052-9) (1985).
- 52 Yin, S. *et al.* Deposition behavior of thermally softened copper particles in cold spraying. *Acta Materialia* **61**, 5105-5118, doi:<https://doi.org/10.1016/j.actamat.2013.04.041> (2013).
- 53 Jian, S. R., Chen, G. J. & Hsu, W. M. Mechanical Properties of Cu₂O Thin Films by Nanoindentation. *Materials (Basel)* **6**, 4505-4513, doi:10.3390/ma6104505 (2013).
- 54 J.K. Lumpp, Nan Chen & K.C. Goretta. Mechanical Properties of CuO. *High Temperature Materials and Processes* **9**, 1-6, doi:doi:10.1515/HTMP.1990.9.1.1 (1990).
- 55 Casellas, D., Nagl, M. M., Llanes, L. & Anglada, M. Fracture toughness of alumina and ZTA ceramics: microstructural coarsening effects. *Journal of Materials Processing Technology* **143-144**, 148-152, doi:[https://doi.org/10.1016/S0924-0136\(03\)00396-0](https://doi.org/10.1016/S0924-0136(03)00396-0) (2003).
- 56 Saeki, I. *et al.* Measurement of Young's modulus of oxides at high temperature related to the oxidation study. *Materials at High Temperatures* **28**, 264-268, doi:10.3184/096034011X13182685579795 (2011).
- 57 Chicot, D. *et al.* Mechanical properties of magnetite (Fe₃O₄), hematite (α -Fe₂O₃) and goethite (α -FeO·OH) by instrumented indentation and molecular dynamics analysis. *Materials Chemistry and Physics* **129**, 862-870, doi:<https://doi.org/10.1016/j.matchemphys.2011.05.056> (2011).
- 58 Tromans, D. & Meech, J. A. Fracture toughness and surface energies of minerals: theoretical estimates for oxides, sulphides, silicates and halides. *Minerals Engineering* **15**, 1027-1041, doi:[https://doi.org/10.1016/S0892-6875\(02\)00213-3](https://doi.org/10.1016/S0892-6875(02)00213-3) (2002).
- 59 Ren, B. & Song, J. Peridynamic Simulation of Particles Impact and Interfacial Bonding in Cold Spray Process. *Journal of Thermal Spray Technology* **31**, 1827-1843, doi:10.1007/s11666-022-01409-w (2022).
- 60 Rahmati, S. & Jodoin, B. Physically Based Finite Element Modeling Method to Predict Metallic Bonding in Cold Spray. *Journal of Thermal Spray Technology* **29**, 611-629, doi:10.1007/s11666-020-01000-1 (2020).
- 61 Profizi, P., Combescure, A. & Ogawa, K. SPH modeling of adhesion in fast dynamics: Application to the Cold Spray process. *Comptes Rendus Mécanique* **344**, 211-224, doi:<https://doi.org/10.1016/j.crme.2016.02.001> (2016).
- 62 Chakrabarty, R. & Song, J. A modified Johnson-Cook material model with strain gradient plasticity consideration for numerical simulation of cold spray process. *Surface and*

- Coatings Technology* **397**, 125981, doi:<https://doi.org/10.1016/j.surfcoat.2020.125981> (2020).
- 63 Meng, F., Hu, D., Gao, Y., Yue, S. & Song, J. Cold-spray bonding mechanisms and deposition efficiency prediction for particle/substrate with distinct deformability. *Materials & Design* **109**, 503-510, doi:<https://doi.org/10.1016/j.matdes.2016.07.103> (2016).
- 64 Meng, F., Yue, S. & Song, J. Quantitative prediction of critical velocity and deposition efficiency in cold-spray: A finite-element study. *Scripta Materialia* **107**, 83-87, doi:<https://doi.org/10.1016/j.scriptamat.2015.05.026> (2015).
- 65 Silling, S. A. & Askari, E. A meshfree method based on the peridynamic model of solid mechanics. *Computers & Structures* **83**, 1526-1535, doi:<https://doi.org/10.1016/j.compstruc.2004.11.026> (2005).
- 66 Madenci, E. & Oterkus, E. in *Peridynamic theory and its applications* 19-43 (Springer, 2013).
- 67 Madenci, E. & Oterkus, S. Ordinary state-based peridynamics for plastic deformation according to von Mises yield criteria with isotropic hardening. *Journal of the Mechanics and Physics of Solids* **86**, 192-219, doi:<https://doi.org/10.1016/j.jmps.2015.09.016> (2016).
- 68 Tiamiyu, A. A. *et al.* Oxide layer delamination: An energy dissipation mechanism during high-velocity microparticle impacts. *Applied Surface Science* **574**, 151673, doi:<https://doi.org/10.1016/j.apsusc.2021.151673> (2022).
- 69 Tiamiyu, A. A., Sun, Y., Nelson, K. A. & Schuh, C. A. Site-specific study of jetting, bonding, and local deformation during high-velocity metallic microparticle impact. *Acta Materialia* **202**, 159-169, doi:<https://doi.org/10.1016/j.actamat.2020.10.057> (2021).
- 70 Hassani-Gangaraj, M., Veysset, D., Nelson, K. A. & Schuh, C. A. Impact-bonding with aluminum, silver, and gold microparticles: Toward understanding the role of native oxide layer. *Applied Surface Science* **476**, 528-532, doi:<https://doi.org/10.1016/j.apsusc.2019.01.111> (2019).
- 71 Li, W.-Y., Li, C.-J. & Liao, H. Significant influence of particle surface oxidation on deposition efficiency, interface microstructure and adhesive strength of cold-sprayed copper coatings. *Applied Surface Science* **256**, 4953-4958, doi:<https://doi.org/10.1016/j.apsusc.2010.03.008> (2010).
- 72 Klinkov, S. V., Kosarev, V. F. & Rein, M. Cold spray deposition: Significance of particle impact phenomena. *Aerospace Science and Technology* **9**, 582-591, doi:<https://doi.org/10.1016/j.ast.2005.03.005> (2005).
- 73 Stoltenhoff, T., Kreye, H. & Richter, H. J. An analysis of the cold spray process and its coatings. *Journal of Thermal Spray Technology* **11**, 542-550, doi:10.1361/105996302770348682 (2002).
- 74 Dowding, I. *et al.* Particle size effects in metallic microparticle impact-bonding. *Acta Materialia* **194**, 40-48, doi:<https://doi.org/10.1016/j.actamat.2020.04.044> (2020).
- 75 Van Steenkiste, T. H., Smith, J. R. & Teets, R. E. Aluminum coatings via kinetic spray with relatively large powder particles. *Surface and Coatings Technology* **154**, 237-252, doi:[https://doi.org/10.1016/S0257-8972\(02\)00018-X](https://doi.org/10.1016/S0257-8972(02)00018-X) (2002).
- 76 Li, W.-Y. *et al.* On high velocity impact of micro-sized metallic particles in cold spraying. *Applied Surface Science* **253**, 2852-2862, doi:<https://doi.org/10.1016/j.apsusc.2006.05.126> (2006).

- 77 Hassani-Gangaraj, M., Veysset, D., Champagne, V. K., Nelson, K. A. & Schuh, C. A. Adiabatic shear instability is not necessary for adhesion in cold spray. *Acta Materialia* **158**, 430-439, doi:<https://doi.org/10.1016/j.actamat.2018.07.065> (2018).
- 78 Bae, G., Xiong, Y., Kumar, S., Kang, K. & Lee, C. General aspects of interface bonding in kinetic sprayed coatings. *Acta Materialia* **56**, 4858-4868, doi:<https://doi.org/10.1016/j.actamat.2008.06.003> (2008).
- 79 Dykhuizen, R. C. *et al.* Impact of high velocity cold spray particles. *Journal of Thermal Spray Technology* **8**, 559-564, doi:10.1361/105996399770350250 (1999).